

See discussions, stats, and author profiles for this publication at: <https://www.researchgate.net/publication/228725538>

# Numerical Study of the Size-Dependent Melting Mechanisms of Nickel Nanoclusters

ARTICLE *in* THE JOURNAL OF PHYSICAL CHEMISTRY C · FEBRUARY 2009

Impact Factor: 4.77 · DOI: 10.1021/jp8058992

---

CITATIONS

45

---

READS

78

## 2 AUTHORS:



**Erik C. Neyts**

University of Antwerp

110 PUBLICATIONS 1,590 CITATIONS

SEE PROFILE



**Annemie Bogaerts**

University of Antwerp

465 PUBLICATIONS 7,134 CITATIONS

SEE PROFILE

# Numerical Study of the Size-Dependent Melting Mechanisms of Nickel Nanoclusters

Erik C. Neyts\* and Annemie Bogaerts

Research Group PLASMANT, Department of Chemistry, University of Antwerp, Universiteitsplein 1, 2610 Antwerp, Belgium

Received: July 04, 2008; Revised Manuscript Received: December 03, 2008

Molecular dynamics simulations were used to investigate the size-dependent melting mechanism of nickel nanoclusters of various sizes. The melting process was monitored by the caloric curve, the overall cluster Lindemann index, and the atomic Lindemann index. Size-dependent melting temperatures were determined, and the correct linear dependence on inverse diameter was recovered. We found that the melting mechanism gradually changes from dynamic coexistence melting to surface melting with increasing cluster size. These findings are of importance in better understanding carbon nanotube growth by catalytic chemical vapor deposition as the phase state of the catalyst nanoparticle codetermines the growth mechanism.

## Introduction

The unique electronic, mechanical, and optical properties of carbon nanotubes (CNTs) render these materials excellent candidates for applications in numerous fields, including microelectronics, medical applications, and materials science.<sup>1,2</sup> However, their applicability is currently limited because of their production costs, the polydispersity in nanotube types, and limitations on processing methods.<sup>3</sup> Clearly, a fundamental understanding of their growth mechanisms in the different production methods would help to overcome these barriers.

One widely used technique for the production of carbon nanotubes is catalytic chemical vapor deposition (CCVD). In CCVD, a feedstock of hydrocarbon gas (such as CH<sub>4</sub>, C<sub>2</sub>H<sub>2</sub>, etc.) is catalytically decomposed in the presence of metal catalyst nanoparticles (e.g., Ni, Fe, Co, FeMo).<sup>4–7</sup> Both the thermodynamic state of the catalyst<sup>8</sup> and the carbon diffusion from the decomposition site to the growing CNT<sup>9</sup> are believed to be important factors in determining the growth mechanism and the properties of the resulting CNTs.

Two qualitative models for the growth of CNTs have been proposed. In the vapor–liquid–solid (VLS) model,<sup>10</sup> the catalyst particle is in the liquid state, which allows rapid diffusion of carbon atoms throughout the particle. Another mechanism, the surface-mediated carbon transport model,<sup>11,12</sup> has been proposed to explain the low-temperature nanotube growth by plasma-enhanced CVD (PECVD). Indeed, the low-temperature PECVD conditions imply that the catalyst is in a solid state, rather than in a liquid state as assumed in the VLS model. Hence, it is clearly of great importance to obtain better insight into the melting behavior of the catalyst particles in order to understand CNT growth.

The melting temperature of free nanosized clusters has been investigated by several authors both experimentally<sup>13–15</sup> and computationally<sup>16–22</sup> for several different materials. Already in 1909, Pawlow suggested the lowering of the melting temperature of small clusters compared to bulk material.<sup>23</sup> More recently, it has been further established that the cluster melting temperature decreases linearly with inverse cluster diameter,<sup>13,16–19</sup> except

TABLE 1: Numbers of Atoms, Diameters, and Inverse Diameters of the Investigated Clusters

cluster	diameter (nm)	inverse diameter (nm <sup>−1</sup> )
Ni <sub>90</sub>	1.23	0.81
Ni <sub>117</sub>	1.35	0.74
Ni <sub>170</sub>	1.53	0.66
Ni <sub>244</sub>	1.72	0.58
Ni <sub>293</sub>	1.83	0.55
Ni <sub>377</sub>	1.99	0.50

for a few notable exceptions, such as Na and small Al, Ga, and Sn clusters (containing 10–30 atoms).<sup>24</sup>

The simulation of the melting of nickel nanoclusters has been studied previously both for very small clusters (containing 7–23 atoms), by Nayak et al. using tight-binding molecular dynamics (MD)<sup>20</sup> and by Lee et al. using tight-binding Monte Carlo (MC),<sup>25</sup> and for medium-sized clusters (containing 336–8007 atoms), by Qi et al. using a Sutton–Chen (including quantum corrections, Q-SC) potential.<sup>26</sup> However, single-walled carbon nanotubes (SWNTs) are mostly grown from metal particles with sizes of ~0.6–2.1 nm,<sup>16</sup> which, in the case of nickel, corresponds to 20–500 atoms. To the best of our knowledge, simulation data on the size-dependent melting behavior of Ni nanoclusters of these sizes remains unreported. The focus of this work is therefore on the melting behavior of nickel clusters containing 90–377 atoms, corresponding to sizes in the range applicable for SWNT growth.

Indeed, because the melting behavior of metal nanoclusters is very much dependent on their size, it is of great importance to understand in detail the melting mechanisms in this range of cluster sizes if SWNT nucleation is to be understood.

## Simulation Setup

The simulation procedure consists of two stages. In the first stage, six initial configurations were constructed, corresponding to six different cluster sizes, as summarized in Table 1. To avoid excessive temperature fluctuations in the MD simulations of the nanoparticles, it is recommended that one start from the most stable configurations,<sup>17</sup> both in configuration space and in momentum space. These stable configurations were obtained by first generating liquid nickel nanoclusters using a combined

\* Corresponding author. Tel.: +32-3-820.23.82. Fax: +32-3-820.23.76. E-mail: erik.neyts@ua.ac.be.

Monte Carlo–molecular dynamics procedure, followed by annealing of the nanoparticles for  $3 \times 10^6$  MD iterations (see below).

Energies and forces were calculated using a recently developed many-body interatomic potential.<sup>27–29</sup> In this potential, the total binding energy is defined as a sum over atomic sites  $i$

$$E_b = \frac{1}{2} \sum_i E_i \quad (1)$$

where each contribution  $E_i$  is written as

$$E_i = \sum_{j \neq i} V_R(r_{ij}) - V_A(r_{ij}) \quad (2)$$

Here,  $V_R$  and  $V_A$  are pair-additive repulsive and attractive Morse-type functions, respectively

$$V_R(r_{ij}) = \frac{D_e}{S-1} \exp[-\beta\sqrt{2S}(r_{ij} - R_e)]$$

$$V_A(r_{ij}) = B^* \frac{D_e S}{S-1} \exp[-\beta\sqrt{2S}(r_{ij} - R_e)] \quad (3)$$

where  $r_{ij}$  denotes the distance between two metal atoms;  $D_e$  and  $R_e$  are the binding energy and equilibrium bond length, respectively; and the parameters  $S$  and  $\beta$  determine the shape of the potential functions. In the case of metal–metal interactions, the binding energy,  $D_e$ , and the equilibrium bond length,  $R_e$ , are expressed as direct functions of the metal coordination number,  $N^M$ , thereby effectively modeling the many-body effects

$$D_e = D_{e1} + D_{e2} \exp[-C_D(N_{ij}^M - 1)]$$

$$R_e = R_{e1} + R_{e2} \exp[-C_R(N_{ij}^M - 1)] \quad (4)$$

As this potential was developed to investigate carbon nano-tube functions, functions are also included for the carbon–metal interactions. (A simplified Brenner potential is used to model the carbon–carbon interactions.<sup>30</sup>) For the carbon–metal interactions, the many-body effect is modeled through the additional  $B^*$  term, which is expressed as a function of the carbon coordination number,  $N^C$ , of a metal atom

$$B^* = [1 + b(N^C - 1)]^\delta \quad (5)$$

The coordination numbers  $N^C$  and  $N^M$  are defined using a cutoff function  $f(r_{ij})$

$$f(r_{ij}) = \begin{cases} 1 & (r_{ij} < R_1) \\ \frac{1}{2} \left[ 1 + \cos\left(\frac{r_{ij} - R_1}{R_2 - R_1} \pi\right) \right] & (R_1 < r_{ij} < R_2) \\ 0 & (r_{ij} > R_2) \end{cases} \quad (6)$$

**TABLE 2: Potential Parameters for Ni–Ni Interactions**

parameter	value	parameter	value
$S$	1.3	$R_{e1}$ (eV)	2.4934
$\beta$ (1/Å)	1.5700	$R_{e2}$ (eV)	0.1096
$D_{e1}$ (eV)	0.4217	$C_R$	0.3734
$D_{e2}$ (eV)	1.0144	$R_1$ (Å)	2.7
$C_D$	0.8268	$R_2$ (Å)	3.2

**TABLE 3: Potential Parameters for Ni–C Interactions**

parameter	value	parameter	value
$D_e$ (eV)	2.4673	$R_1$ (Å)	2.7
$S$	1.3	$R_2$ (Å)	3.0
$\beta$ (1/Å)	1.8706	$b$	0.0688
$R_e$ (Å)	1.7628	$\delta$	−0.5351

$$N_i^C = 1 + \sum_{\text{carbon } k (\neq i)} f(r_{ik}) \quad (7)$$

$$N_i^M = 1 + \sum_{\text{metal } k (\neq i)} f(r_{ik}), \quad N_{ij}^M = \frac{N_i^M + N_j^M}{2} \quad (8)$$

The parameters for the Ni–Ni interactions are given in Table 2. The parameters for the Ni–C interactions, although not used for the present simulations, are given for the sake of completeness in Table 3.

Although other interatomic potentials are available for studying the thermal behavior of nickel nanoclusters, including, for example, the embedded-atom method (EAM),<sup>31</sup> the modified EAM (MEAM),<sup>32</sup> and the Finnis–Sinclair potentials,<sup>33</sup> these potentials do not include terms allowing for simulating Ni-catalyzed CNT growth. Because this is the final aim of our research, it is most appropriate to study the thermal behavior of the nickel nanoclusters using the same potential.

The liquid nanoclusters were obtained by first creating fcc-structured nanocrystals, which were propagated by force-biased Monte Carlo<sup>34</sup> (fbMC) for  $1 \times 10^6$  steps at a temperature of 2000 K, well above the bulk melting temperature of nickel (i.e., 1724 K).

In the fbMC algorithm, all atoms are displaced in the direction of the force, modified by a temperature-dependent random component. In each direction  $r$ , the length of the displacement  $\delta_r$ , is calculated as<sup>34</sup>

$$\delta_r = \frac{2k_B T}{F_r} \ln \left[ \frac{1}{\alpha} + \left( \alpha - \frac{1}{\alpha} \right) R \right] \quad (9)$$

where  $R$  is a random number,  $F_r$  is the force component along  $r$ , and  $\alpha$  is defined as

$$\alpha = \exp \left( \frac{|\epsilon F_r|}{2k_B T} \right) \quad (10)$$

with  $\epsilon$  being a predefined value fixing the maximum displacement length in each direction. In this work, a value equal to 5% of the average bond length was chosen. From these definitions, it follows that

$$\lim_{\ln(\alpha) \rightarrow 0} \delta_r = (1 - 2R)\epsilon \quad (11a)$$

$$\lim_{\ln(\alpha) \rightarrow \infty} \delta_r = \pm \varepsilon \quad (11b)$$

Hence, for high temperatures or small forces (eq 11a), atoms are displaced in random directions, whereas for low temperature or large forces (eq 11b), atoms are displaced in the direction of the force. Contrary to the metropolis MC algorithm, each atomic move is accepted in this algorithm. This procedure ensures that the positions of the atoms in the nanoclusters correspond to a liquid state.

To ensure that the velocities also correspond to the correct canonical ensemble of liquid nickel, the resulting structures were equilibrated for  $2 \times 10^6$  MD steps using the Andersen heat bath<sup>35</sup> with a time step of 0.5 fs. This corresponds to the first annealing step. The coupling to the heat bath is represented by stochastic impulsive forces that act with a predefined frequency on randomly chosen atoms. These stochastic “collisions” ensure that all accessible constant-energy configurations are visited according to their respective Boltzmann weights, effectively resulting in sampling of the canonical ensemble.<sup>36,37</sup> Finally, the equilibrated structures were cooled to 500 K during  $1 \times 10^6$  MD time steps, again using the Andersen heat bath, corresponding to the second annealing step.

In the second stage of this simulation procedure, the melting mechanism of the obtained nanoclusters was monitored by heating the clusters consecutively to increasing temperatures in the range of 600–1750 K. At each temperature, the configuration was heated for  $4 \times 10^5$  iterations with a time step of 0.5 fs, followed by  $6 \times 10^6$  iterations without temperature control and a time step of 0.25 fs, ensuring energy conservation to at least  $(1 \times 10^{-4})\%$ .

All MD trajectories were propagated using the symplectic velocity Verlet algorithm.<sup>38</sup> The properties used to monitor the melting behavior (i.e., the overall Lindemann index, the Lindemann indices of all atoms, and the caloric curve) are recorded during the last  $5 \times 10^6$  iterations. The resulting configuration was then used as input for the next simulation at a higher temperature, with an interval of 50 K.

Note that the Andersen heat bath is a stochastic method, and hence, the temperature could not be controlled exactly. To (partially) resolve the resulting gaps in the obtained temperatures, all melting simulations (stage 2) were carried out twice, and the data were combined. A second problem associated with using the Andersen heat bath is that, on some occasions, the temperature of a new configuration (i.e., after the heating) is lower than the temperature of the configuration that was used as input (i.e., before the heating), especially in the smallest clusters. Because these configurations correspond to a solidification process instead of a melting process and because the corresponding phase transitions do not coincide,<sup>18</sup> their data were removed from the final data set.

### Definition of Melting Point

The melting behavior of the clusters was monitored by the variation of the overall cluster Lindemann index with respect to temperature,<sup>39</sup> the variation of the individual atomic Lindemann indices with respect to temperature, and the variation of the total energy with temperature (i.e., the caloric curve). The Lindemann index represents the root-mean-square relative bond length fluctuation

$$\delta_i = \frac{1}{N-1} \sum_{j \neq i} \frac{\sqrt{\langle r_{ij}^2 \rangle_T - \langle r_{ij} \rangle_T^2}}{\langle r_{ij} \rangle_T} \quad (12)$$

$$\delta_{cl} = \frac{1}{N} \sum_i \delta_i \quad (13)$$

where  $\delta_i$  and  $\delta_{cl}$  are the Lindemann indices of the  $i$ th atom and the overall cluster, respectively;  $\langle \dots \rangle_T$  denotes the thermal average at temperature  $T$ ;  $r_{ij}$  is the distance between atoms  $i$  and  $j$ ; and  $N$  is the number of atoms in the cluster. In the literature, different criteria have been used to determine the melting point, corresponding to average Lindemann indices ranging from 0.03 for CNTs<sup>40</sup> to 0.24.<sup>26</sup> Most often, however, a value in the range of 0.08–0.15 is used for various nanocluster materials.<sup>18,21,41,42</sup> In this work, we employed a critical value of 0.08.<sup>42</sup> Note that the melting point is, in fact, a macroscopic concept, defined as the temperature at which a solid becomes liquid. Because of the finite size, however, melting occurs over a range of temperatures, in which the solid and liquid phases can coexist with different fractions.<sup>43</sup> To obtain a specific point instead of a range of temperatures, we therefore defined the melting temperature in this work as the temperature at which the melting process starts, i.e., the lowest temperature at which the solid and liquid phases coexist (the so-called min-liquid point<sup>17</sup>), which, in the current system, indeed corresponds to a Lindemann value of about 0.08 (see below).

### Results and Discussion

In Figure 1, an example is shown of the evolution of the overall cluster Lindemann index (upper curve) and the total energy (lower curve) as a function of the temperature for a cluster containing 244 atoms. Both properties first increase linearly with increasing temperature, because of the linear increase in atomic kinetic energy. In this temperature region, the atoms are merely vibrating around their equilibrium lattice positions with low amplitude, resulting in a low Lindemann index indicative of a solid structure. With increasing energy, the atoms become increasingly mobile, and the rises in both the Lindemann index and the total energy become nonlinear. At this point, atoms start to show diffusive motion on the MD time scale, and therefore, this indicates the onset of the melting process. To quantify this point, a sixth-order polynomial was fit to the obtained data points of the Lindemann index, and its crossing with the 0.08 boundary was taken as the melting point (indicated by the thin horizontal dashed line in the upper curve of Figure 1). As an alternative to this criterion, a linear fit to the low-temperature caloric curve data was used to identify the first data point for which an appreciable deviation from the linear increase in the caloric curve can be observed (appreciable being 5%). In the figure, this is indicated by the solid straight line in the lower curve.

Both methods were applied to all clusters, and the obtained melting points are plotted in Figure 2 as a function of  $N^{-1/3}$ , with  $N$  being the number of atoms in the cluster. It is clear that both methods give the correct linear dependence on the inverse diameter of the clusters (because  $N^{-1/3}$  is proportional to the inverse diameter), in agreement with both experimental<sup>13,44</sup> and computational<sup>17,26</sup> studies. Note that the melting temperature of bulk nickel can be obtained by extrapolating to  $N \rightarrow \infty$ . The extrapolation based on the Lindemann index data yields a bulk melting temperature of 2076 K, whereas the extrapolation based on the caloric curve data results in a value of 1956 K. These

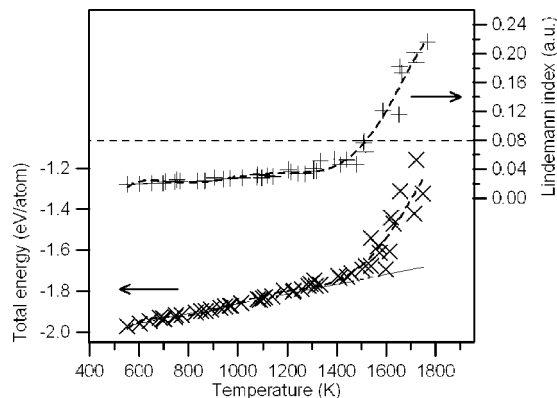


**Figure 1.** Calculated evolution of the overall cluster Lindemann index (upper curve) and the total energy (lower curve) as a function of temperature. The dashed horizontal line in the upper part of the graph indicates the critical boundary value for determination of the melting point using the Lindemann index (see text). The solid line in the lower curve is a linear fit to the low-temperature data of the total energy, also to determine the melting point (see text).

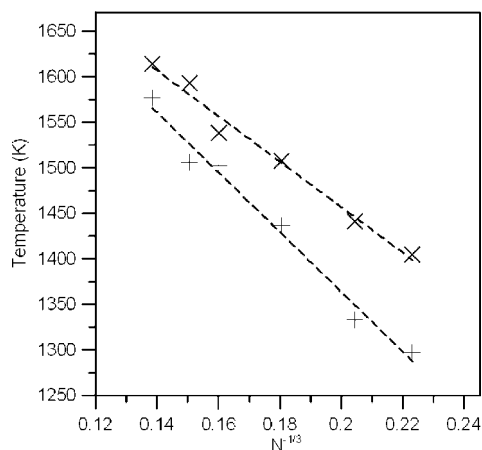


**Figure 2.** Calculated melting points for the investigated clusters of different sizes, based on the cluster Lindemann index (+, lower line) and the total energy (x, upper line).

values are about 19% and 13% higher than the experimental bulk melting temperature of nickel of 1724 K, indicating that the interatomic many-body potential used in our simulations is slightly overbinding.

The melting process was also followed by monitoring the Lindemann indices of individual atoms as a function of their distance to the center of mass of the cluster, as shown in Figure 3 for the cluster containing 244 atoms. These indices indicate the extent to which each atom contributes to the phase state of the cluster. At a temperature of 1420 K, i.e., well below the cluster melting temperature (calculated as 1519 K based on the overall Lindemann index), less than 1% of the atoms have a Lindemann index above the threshold value of 0.08 (see lower panel). At a temperature of 1490 K, close to the melting temperature, about 14% of the atoms have reached the threshold value, although most atoms still have a value slightly below 0.05. Hence, at this temperature, the cluster as a whole is still in the solid phase, although some diffusive motion is occurring at the surface of the cluster (middle panel). Finally, at a temperature of 1560 K, i.e., just above the melting temperature, more than 40% of the atoms have crossed the 0.08 boundary, and all other atoms have a value very close to that boundary. Correspondingly, the diameter of the cluster has increased by more than 10%. Hence, at this temperature, the cluster can be

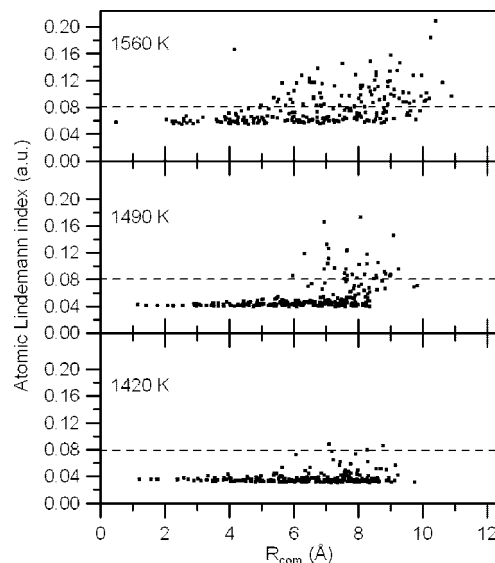


**Figure 3.** Calculated radial distribution of the atomic Lindemann index for a  $\text{Ni}_{244}$  cluster at three different temperatures. Each dot represents a specific atom. For clusters of this size and larger, surface melting is typically observed (note the increasing scatter with increasing temperature for the atoms farthest from the center of mass).

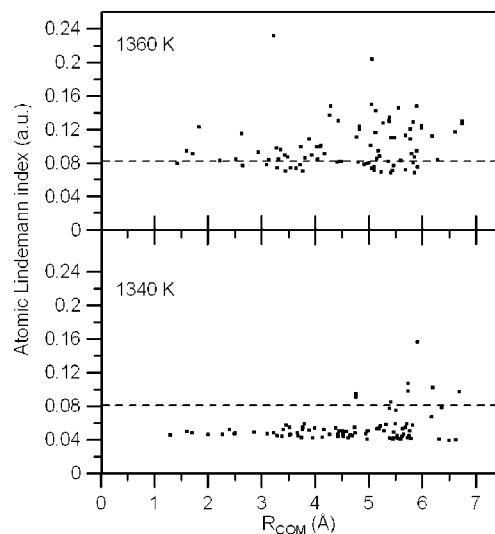


**Figure 4.** Calculated radial distribution of the atomic Lindemann index for a  $\text{Ni}_{90}$  cluster for two temperatures. For clusters of this size, dynamic coexistence melting is observed.

considered to be melting (upper panel). From this evolution, it can be concluded that, for clusters of this size, the melting process can be described as surface melting, in agreement with other studies.<sup>19,21</sup> We observed the same behavior for larger clusters as well. Hence, the CNT growth mechanism operative under these conditions is most likely to be the surface-mediated carbon transport mechanism. Indeed, at temperatures just above the onset of surface melting, the carbon atoms can easily diffuse toward the growing CNT by surface diffusion. At higher temperatures, the bulk of the cluster will also start to melt, and then, the VLS model will be more applicable to describe the CNT growth.

An entirely different mechanism was observed for small clusters, as exemplified in Figure 4 for the cluster of 1.2-nm diameter (i.e., containing 90 atoms). In the lower panel, the atomic Lindemann index is plotted as a function of distance of the atoms to the center of mass of the cluster for a temperature of 1340 K. It is clear that, at this temperature, nearly all atoms



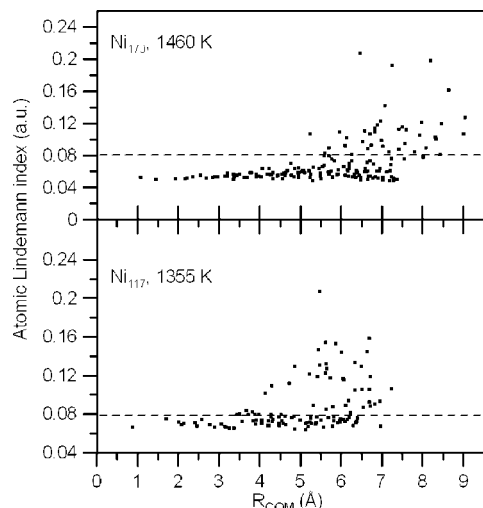


**Figure 5.** Calculated radial distributions of the atomic Lindemann index for Ni<sub>117</sub> and Ni<sub>170</sub> clusters at temperatures about 25 K above their respective melting temperatures. In these medium-sized clusters, the melting mechanism changes gradually from dynamic coexistence melting to surface melting.

have a Lindemann index below the threshold value of 0.08. At a temperature of 1360 K (upper panel), however, nearly all atoms have surpassed the boundary value of 0.08, including the atoms near the center of mass of the cluster, as can be seen from the scatter. Hence, in this temperature region, the overall average Lindemann index also fluctuates heavily, because of the dynamic equilibrium of the liquid and solid states. This phenomenon is known as dynamic coexistence melting.<sup>17,45</sup> The ratio between the two states is given by  $K = \exp(-\Delta G/kT)$ , where  $\Delta G$  is the free energy difference between the solid and liquid phases of the nanoparticle.<sup>46</sup> In this regime, the particles are quasiplastic<sup>17,47</sup> and show continuously alternating metastable semisolid and liquid configurations.

In terms of CNT growth, this phase state of the catalyst could allow the formation of a liquidlike metal carbide particle, as required by the VLS model. Analysis of the other clusters studied in this work revealed a gradual change from the dynamic coexistence melting mechanism to the surface melting mechanism with increasing cluster size. Indeed, it can be seen from Figure 5 that, at a temperature just above its melting temperature, the Ni<sub>117</sub> cluster contains far more atoms near its centroid with a Lindemann index above and very close to the threshold value of 0.08 than does the Ni<sub>170</sub> cluster. Hence, as the cluster size increases from 90 to 117 to 170 to 240, it can be seen that, above the melting point, when the cluster starts to melt, the ratio of the surface atoms to the total number of atoms with Lindemann indices above the threshold value increases gradually. Therefore, whereas the smallest cluster shows dynamic coexistence melting and the largest cluster shows pure surface melting, there is a gradual transition between the two modes for clusters with intermediate sizes.

## Conclusion

Molecular dynamics simulations using a recently developed interatomic many-body potential were carried out to investigate the melting mechanism of nickel nanoclusters with diameters between 1 and 2 nm, which are typically used for the catalytic growth of single-walled carbon nanotubes. The melting process was followed by monitoring the cluster Lindemann index, the caloric curve, and the atomic Lindemann indices of each investigated cluster. In agreement with the literature, a linear

decrease in melting temperature was found with increasing inverse diameter. A gradual transition from a dynamic coexistence melting mechanism for the smallest clusters (diameter  $\approx$  1 nm) to a surface melting mechanism for the larger clusters (diameter  $\approx$  2 nm) was observed. It is therefore expected that the vapor–liquid–solid growth mechanism will be operative for SWNT growth from the smallest nanoparticles and from larger catalyst particles at higher temperatures, whereas the surface-mediated carbon transport model should be more appropriate for describing SWNT growth from larger particles at lower temperatures. These results should be of importance for understanding the catalytic nucleation process of SWNTs from nickel clusters with sizes between 1 and 2 nm.

**Acknowledgment.** E. C. N. acknowledges the FWO-Flanders (Fund for Scientific Research-Flanders) for financial support and the core facility CALCUA for calculation support, provided by the University of Antwerp. This research was also sponsored by the Prime Minister's Office through IAP VI. Finally, the authors also gratefully acknowledge useful discussions with Y. Shibuta.

## References and Notes

- (1) Saito, R.; Dresselhaus, G.; Dresselhaus, M. S. *Physical Properties of Carbon Nanotubes*; Imperial College Press, London, 1998.
- (2) Meyyappan, M.; Delzeit, L.; Cassell, A.; Hash, D. *Plasma Sources Sci. Technol.* **2003**, *12*, 205.
- (3) Baughman, R. H.; Zakhidov, A. A.; de Heer, W. A. *Science* **2002**, *297*, 787.
- (4) Kong, J.; Soh, H. T.; Cassell, A. M.; Quate, C. F.; Dai, H. *Nature* **1998**, *395*, 878.
- (5) Geohagan, D. B.; Puzos, A. A.; Ivanov, I. N.; Jesse, S.; Eres, G.; Howe, J. Y. *Appl. Phys. Lett.* **2003**, *93*, 1851.
- (6) Harutyunyan, A. R.; Pradhan, B. K.; Kim, U. J.; Chen, G.; Eklund, P. C. *Nano Lett.* **2002**, *2*, 525.
- (7) Dupuis, A.-C. *Prog. Mater. Sci.* **2005**, *50*, 929.
- (8) Harutyunyan, A. R.; Tokune, T.; Mora, E. *Appl. Phys. Lett.* **2005**, *87*, 051919.
- (9) Hofmann, S.; Csányi, G.; Ferrari, A. C.; Payne, M. C.; Robertson, J. *Phys. Rev. Lett.* **2005**, *95*, 036101.
- (10) Wagner, R. S.; Ellis, W. C. *Appl. Phys. Lett.* **1964**, *4*, 89.
- (11) Helveg, S.; López-Cartes, C.; Sehested, J.; Hansen, P. L.; Clausen, B. S.; Rostrup-Nielsen, J. R.; Abild-Pedersen, F.; Nørskov, J. K. *Nature* **2004**, *427*, 426.
- (12) Abild-Pedersen, F.; Nørskov, J. K.; Rostrup-Nielsen, J. R.; Sehested, J.; Helveg, S. *Phys. Rev. B* **2006**, *73*, 115419.
- (13) Buffat, P. A.; Borel, J. P. *Phys. Rev. A* **1976**, *13*, 2287.
- (14) Haberland, H.; Hippler, T.; Donges, J.; Kostko, O.; Schmidt, M.; von Issendorff, B. *Phys. Rev. Lett.* **2005**, *79*, 035701.
- (15) Bachelis, T.; Güntherodt, H.-J. *Phys. Rev. Lett.* **2000**, *85*, 1250.
- (16) Bolton, K.; Ding, F.; Rosén, A. *J. Nanosci. Nanotechnol.* **2006**, *6*, 1211.
- (17) Jiang, A.; Awasthi, N.; Kolmogorov, A. N.; Setyawan, W.; Börjesson, A.; Bolton, K.; Harutyunyan, A. R.; Curtarolo, S. *Phys. Rev. B* **2007**, *75*, 205426.
- (18) Shibuta, Y.; Suzuki, T. *Chem. Phys. Lett.* **2007**, *445*, 265.
- (19) Duan, H.; Ding, F.; Rosén, A.; Harutyunyan, A. R.; Curtarolo, S.; Bolton, K. *Chem. Phys.* **2007**, *333*, 57.
- (20) Nayak, S. K.; Khanna, S. N.; Rao, B. K.; Jena, P. *J. Phys.: Condens. Matter* **1998**, *10*, 10853.
- (21) Ding, F.; Bolton, K.; Rosén, A. *Eur. Phys. J. D* **2005**, *34*, 275.
- (22) Proykova, A.; Pisov, S.; Berry, R. S. *J. Chem. Phys.* **2001**, *115*, 8583.
- (23) Pawlow, P. *Phys. Z. Stoechiom. Verwandtschaftsl.* **1909**, *65*, 545.
- (24) Baletto, F.; Ferrando, R. *Rev. Mod. Phys.* **2005**, *77*, 371–423.
- (25) Lee, Y. J.; Maeng, J. Y.; Lee, E.-K.; Kim, B.; Kim, S.; Han, K.-K. *J. Comput. Chem.* **2000**, *21*, 380.
- (26) Qi, Y.; Çagin, T.; Johnson, W. L.; Goddard, W. A., III *J. Chem. Phys.* **2001**, *115*, 385.
- (27) Yamaguchi, Y.; Maruyama, S. *Eur. Phys. J. D* **1999**, *9*, 385–388.
- (28) Shibuta, Y.; Maruyama, S. *Chem. Phys. Lett.* **2007**, *437*, 218–223.
- (29) Shibuta, Y.; Maruyama, S. *Comput. Mater. Sci.* **2007**, *39*, 842.
- (30) Yamaguchi, Y.; Maruyama, S. *Chem. Phys. Lett.* **1998**, *286*, 336–342.
- (31) Daw, M. S.; Baskes, M. I. *Phys. Rev. B* **1984**, *29*, 6443–6453.
- (32) Baskes, M. I. *Phys. Rev. B* **1992**, *46*, 2727–2742.

- (33) Dai, X. D.; Kong, Y.; Li, J. H.; Liu, B. X. *J. Phys.: Condens. Matter* **2006**, *18*, 4527–4542.
- (34) Dereli, G. *Mol. Simul.* **1992**, *8*, 351.
- (35) Andersen, H. C. *J. Chem. Phys.* **1980**, *72*, 2384.
- (36) Frenkel, D.; Smit, B. *Understanding Molecular Simulation*, Academic Press: London, 1996.
- (37) Allen, M. P.; Tildesley, D. L. *Computer simulation of liquids*, Oxford University Press: Oxford, U.K., 2003.
- (38) Swope, W. C.; Anderson, H. C.; Berens, P. H.; Wilson, K. R. *J. Chem. Phys.* **1982**, *76*, 637.
- (39) Lindemann, F. A. *Phys. Z.* **1910**, *11*, 609.
- (40) Zhang, K.; Stocks, G. M.; Zhong, J. *Nanotechnology* **2007**, *18*, 285703.
- (41) Börjesson, A.; Curtarolo, S.; Harutyunyan, A. R.; Bolton, K. *Phys. Rev. B* **2008**, *77*, 115450.
- (42) Radev, R.; Proykova, A. *Comput. Phys. Commun.* **2002**, *147*, 242.
- (43) Lupis, C. H. P. *Chemical Thermodynamics of Materials*; North-Holland: New York, 1983.
- (44) Dippel, M.; Maier, A.; Gimple, V.; Wider, H.; Evenson, W. E.; Rasera, R. L.; Schatz, G. *Phys. Rev. Lett.* **2001**, *87*, 095505.
- (45) Alavi, S.; Thompson, D. L. *J. Phys. Chem. A* **2006**, *110*, 1518.
- (46) Alavi, S.; Thompson, D. L. *J. Chem. Phys.* **2004**, *120*, 10231–10239.
- (47) Melnik, R. V. N.; Roberts, A. J.; Thomas, K. A. *Comput. Mech.* **2002**, *29*, 16–26.

JP8058992